Manipulate energy transport via fluorinated spacers towards record-efficiency 2D Dion-Jacobson $CsPbI_3$ solar cells

Lei, Yutian ; Li, Zhen-Hua ; Wang, Haoxu; Wang, Qian; Peng, Guoqiang ; Xu, Youkui ; Zhang, Haihua ; Wang, Gang; Ding, Liming ; Jin, Zhiwen

DOI
10.1016/j.scib.2022.05.019

Publication date
2022

Document Version
Final published version

Published in
Science Bulletin

Science Bulletin 67 (2022) 1352–1361

Contents lists available at ScienceDirect

Science Bulletin

journal homepage: www.elsevier.com/locate/scib

Article

Manipulate energy transport via fluorinated spacers towards record-efficiency 2D Dion-Jacobson $CsPbI_3$ solar cells

Yutian Lei [a,1], Zhenhua Li [b,1], Haoxu Wang [c], Qian Wang [a], Guoqiang Peng [a], Youkui Xu [a], Haihua Zhang [d], Gang Wang [e], Liming Ding [f], Zhiwen Jin [a,*]

[a] School of Physical Science and Technology & Key Laboratory for Magnetism and Magnetic Materials of the Ministry of Education, Lanzhou University, Lanzhou 730000, China
[b] School of Physical Science and Technology & Lanzhou Center for Theoretical Physics & Key Laboratory of Theoretical Physics of Gansu Province, Lanzhou University, Lanzhou 730000, China
[c] Delft University of Technology, Photovoltaic Materials and Devices Group, Delft 2628CD, the Netherlands
[d] Institute of Molecular Plus, Tianjin University, Tianjin 300072, China
[e] Department of Microelectronic Science and Engineering, School of Physical Science and Technology, Ningbo University, Ningbo 315211, China
[f] Key Laboratory of Nanosystem and Hierarchical Fabrication, National Center for Nanoscience and Technology, Beijing 100190, China

ARTICLE INFO

Article history:
Received 10 March 2022
Received in revised form 16 April 2022
Accepted 23 May 2022
Available online 27 May 2022

Keywords:
Dion-Jacobson $CsPbI_3$
Fluorinated spacers
Energy transport
Interaction

ABSTRACT

Two-dimensional (2D) Dion-Jacobson (D-J)-type cesium lead iodide $CsPbI_3$ perform remarkably in terms of stability. However, the complex interactions between spacer and inorganic layers limit its excellent progress in perovskite solar cells (PSCs). Herein, starting from the considerable structural diversity of organic spacers, we engineer 2D $CsPbI_3$ with fine-tuning functionalities. Specifically, for the first time we embedded fluorinated aromatic cations in 2D D-J $CsPbI_3$, and successfully applied it into construction of high-performance PSCs. Compared with constitutive 1,4-diaminobenzene (PDA), the fluorinated 2-fluorobenzene-1,4-diamine (F-PDA) component greatly expands the dipole moment from 0.59D to 3.47D, which reduces the exciton binding energy of the system. A theoretical study shows that the spacer layer and inorganic plane are more enriched with charge accumulation in (F-PDA)$Cs_{n-1}Pb_nI_{3n+1}$. The results show that (F-PDA)$Cs_{n-1}Pb_nI_{3n+1}$ demonstrates more significant charge transfer between organic and inorganic layers than (PDA)$Cs_{n-1}Pb_nI_{3n+1}$, and it is confirmed in the femtosecond transient absorption experiment. Moreover, the interactions of the fluorinated spacer with the $[PbI_6]^{4-}$ plane effectively manipulate the crystallization quality, and thus the ion migration and defect formation of target 2D $CsPbI_3$ are inhibited. As a result, we obtained a record power conversion efficiency (PCE) beyond 15% for 2D D-J (F-PDA)$Cs_3Pb_4I_{13}$ (n = 4) PSCs with significantly improved environmental stability compared with the three-dimensional (3D) counterparts.

1. Introduction

The power conversion efficiency (PCE) of $CsPbI_3$ perovskite solar cells (PSCs) has exceeded 20% [1]. However, the device stability is still in urgent need of progress for the fragility of $CsPbI_3$ phase change in terms of meeting commercialization. Until now, the introduction of ammonium salts to stabilize the resulting structure, or the resulting low-dimensional system, is considered a more successful attempt to solve the problem of device instability [2–4]. Ruddlesden-Popper (R-P) and Dion-Jacobson (D-J) structures are currently the two most common two-dimensional (2D) perovskite structures. Typically, there are undesirable van der Waals gaps in R-P perovskites, where the staggered arrangement of monoamine organic cations can spatially expand the interlayer spacing between adjacent inorganic panels. This leads to deteriorated carrier transport inside the 2D bulk and limited structural durability [5,6]. Comparatively, no van der Waals gap exists in the 2D D-J analogues, and the adjacent octahedron is functioned by strong hydrogen bond, which resulting in shorter distance between the inorganic plates and more rigid structure [7,8].

Inspired by the intrinsic structural superiority of the 2D D-J phase, a series of D-J $CsPbI_3$ devices were proposed. In 2017, Zhao's group [9] added $EDAPbI_4$ to the $CsPbI_3$ structure and found that the introduction of the D-J phase can inhibit the formation of unwanted δ phases. In 2020, Hou's group [10] used diammonium-intercalated $CsPb(I_{0.7}Br_{0.3})_3$ to form a cross-linked heterojunction structure comprising separated 2D (n = 1, 2) and three-dimensional (3D) perovskites. Benefiting from the band

* Corresponding author.
E-mail address: jinzw@lzu.edu.cn (Z. Jin).
[1] These authors attributed equally to this work.

https://doi.org/10.1016/j.scib.2022.05.019
2095-9273/

alignment among 2D/3D structures, the device delivered outstanding PCE as well as ideal light and thermal stability. Most recently, Fang et al. [11] used simulation methods to periodically insert diamine cations between inorganic layers of α-$CsPbI_3$ components. The resultant quasi-2D α-$CsPbI_3$ obtained smaller effective mass than conventional 3D counterparts due to accurate anchor of organic components and inorganic plane.

Nevertheless, it has to be admitted that the PCE of 2D D-J $CsPbI_3$ still lags behind their 3D counterpart. Substantially, in terms of 2D intrinsically structure, this is mainly caused by two aspects: (1) organic cations tail the 3D structure into a multi-quantum well structure with the inorganic layer as the "well" and the organic spacer layer as the "barrier" [12]. In detail, the excitons generated at the inorganic "well" can obtain a greater exciton binding energy than 3D counterparts due to the low-dielectric screening of the surrounding organic spacer cations [13,14]. (2) The free electrons and holes are localized in the conduction band (CB) and valence band (VB) of the $[PbI_6]^{4-}$ plane, respectively, and due to the existence of spacer energy barrier between the two adjacent inorganic planes, the out-of-plane charge transport must overcome the barrier induced by organic layer [15–18]. Therefore, it is an intuitive and reasonable design to alleviate the dielectric mismatch and optimize the thickness of quantum barrier through organic ligand engineering. Furthermore, the appropriate structure of organic cations may cause changes in the electronic coupling between adjacent organic cations and octahedral structure of matrix, which will have a profound impact on the out-of-plane charge transport of the device.

Fortunately, the considerable structural diversity of organic spacers offers unprecedented opportunities to design materials with fine-tuning functionalities. Recently, aromatic diamines have attracted widespread interest as spacers for 2D perovskites. The aromatic spacer cations have delocalized π-electrons on the molecular backbone, which can reduce the dielectric mismatch between the corner-sharing inorganic plate and the adjacent organic spacer layer, thereby weakening the dielectric confinement effect [19–21]. In addition, the more rigid skeleton of the benzene-based aromatic diamine cation results in a better ordered structure relative to aliphatic species, and the free π-electrons of the aromatic core can also enhance the charge transport properties [22,23]. However, the contribution of spacers based on a simple benzene ring structure to the optoelectronic properties of 2D devices is still limited due to the lack of specific functionality [24,25].

Fluorine-containing ammonium salts are widely used in the interface modification of PSCs due to their electronegativity with outstanding stability and electron donor properties [26,27]. Notably, fluorine is the most electronegative element, and its van der Waals radius is similar to that of hydrogen atoms. Therefore, fluorine substitution usually has a high tolerance for structural distortion but greatly improves physical properties [28–30]. Encouraged by this, we hypothesized that introducing fluorine atoms at appropriate positions on the benzene ring to tailor the benzene ring structure will introduce new features, such as increasing the dielectric constant and stiffness of the spacer, and more delocalized positive charges on the aromatic ring. Further, these characteristics allow fine-tuning of the electronic properties of the inorganic layer, including the ability to modulate the strength of the internal electrostatic interaction of the inorganic layer and the hydrogen bond with the surrounding environment, as well as the electronic coupling of the spacer and the octahedron.

Herein, we excavated two aromatic spacer cations, 1,4-diaminobenzene (PDA) and 2-fluorobenzene-1,4-diamine (F-PDA), for 2D D-J $CsPbI_3$ and demonstrated highly efficient PSCs with a nominal n = 4 average composition. To be clear, n = 4 here is not a pure phase, but a mixture of multiple n-values. Theoretical calculations show that 2D D-J $CsPbI_3$ using fluorinated spacers exhibits higher charge density and strong electronic coupling around iodine atoms in the layer. Experimentally, (F-PDA) $Cs_3Pb_4I_{13}$ film exhibits improved film quality, preferred vertical orientation, and the corresponding energy transfer between different layers is more favorable. As a result, the optimized (F-PDA) $Cs_3Pb_4I_{13}$ (n = 4) PSCs achieved a record PCE of 15.12% with significantly improved stability.

2. Experimental

2.1. Materials

Cesium iodide (CsI, ≥99.99%), lead(II) iodide (PbI_2, >99.99%), 1,4-diaminobenzene (PDA), F-PDA, 2,2′,7,7′-tetrakis (*N*,*N*-di-*p*-methoxy phenylamine)-9,9′-spirobifluorene (Spiro-OMeTAD), poly(3,4-ethylenedioxythiophene)/poly(styrenesulfonate) (PEDOT/PSS), and [6,6]-phenyl C61 butyric acid methyl ester (PCBM) were acquired from Xi'an Polymer Light Company. Bis(trifluoromethylsulfonyl) imidelithium salt (Li-TFSI), 4-*tert*-butylpyridine (TBP), chlorobenzene, hydriodic acid (HI 57 wt%), *N*,*N*-dimethylformamide (DMF, 99%), $TiCl_4$ and tris (2-(1*H*-pyrazol-1-yl)-4-*tert*-butylpyridine) cobalt(III) tri[bis(trifluoromethane)sulfonimide] (FK209) were gained from Alfa Aesar. Some other synthesis methods of iodized salt is detailed in the Supplementary materials (online).

2.2. Device fabrication

The purchased FTO glass was ultrasonically cleaned with ethanol and isopropanol for 30 min, then dried with dry air, and treated with O_2 plasma for 10 min. Afterwards, the FTO glasses were immersed in 4.5 mL $TiCl_4$ aqueous solution at 70 °C for 60 min and washed with distilled water and ethanol. The compact TiO_2 film was formed after annealing at 200 °C for 30 min. Then, 100 μL 2D $CsPbI_3$ precursor solution was coated on TiO_2 substrate by one-step spin-coating method at 1000 r/min for 10 s and 3000 r/min for 30 s, respectively. The final films were formed after annealing at 210 °C for 10 min. The annealing time for other layers of film is slightly different. Finally, the hole transport layer (Spiro-OMeTAD) was coated on perovskite film by spin coating at 5000 r/min for 35 s. Finally, thermally evaporated Au (80 nm) was used as top electrodes.

Details on the characterization of the perovskite films and PSCs and the computational method for calculations are provided in the Supplementary materials (online).

3. Result and discussion

The structure of organic cations, especially adjusting the electric dipole moment to change the dielectric constant of the spacer, is an effective strategy for modulating the distribution of 2D perovskite quantum wells. Here, we introduce two aromatic organic spacers, namely PDA and F-PDA obtained by replacing the fluorine atom at the ortho-position. Among them, fluorine atom on F-PDA is obtained by replacing the hydrogen atom on the carbon atom in the PDA by means of single-molecule nucleophilic substitution. After the reaction, the C–F bond length is 1.34 Å with very small change compared to the C–H bond length of 1.09 Å in PDA. First, we applied density functional theory (DFT) to calculate the dipole moments as presented in Fig. 1a. Compared with constitutive PDA, the fluorinated F-PDA component greatly expands the dipole moment from 0.59D to 3.47D (D: a unit used to measure the dipole moment of a chemical bond). It should be pointed out that we compared the rotation angles of different structures through Gaussian simulation and obtained the conformation with the lowest energy in the realistic case as the object of DFT calculation [19].

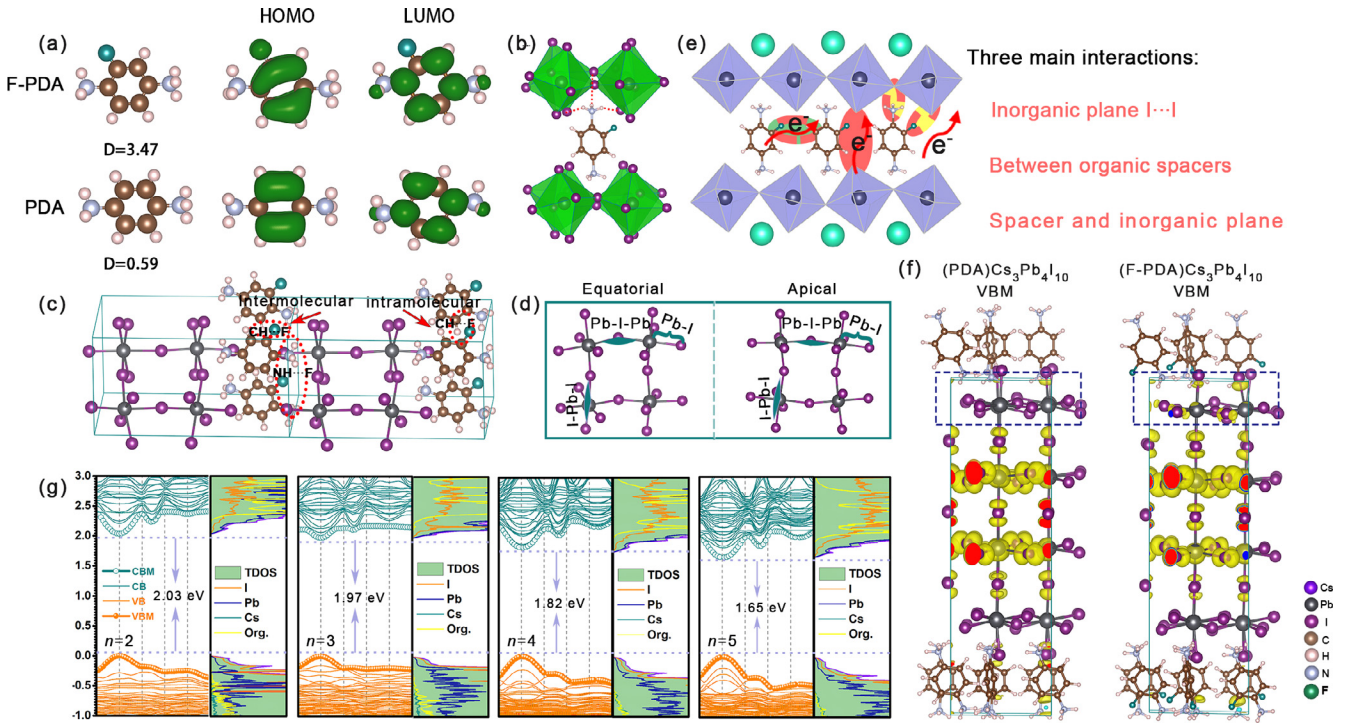

Fig. 1. (Color online) Organic cations and structure simulation of different 2D D-J $CsPbI_3$. (a) Calculated molecular dipole moment of F-PDA^{2+} cation and its electron-density distribution in the lowest unoccupied molecular orbital (LUMO) and highest occupied molecular orbital (HOMO) in comparison to PDA^{2+} cation. (b) The optimized polyhedron model and its partial enlarged drawing. (c) The interaction between organic cations as well as organic cations and inorganic plane in the F-PDA-Pb structure. (d) Definition of equatorial and apical bond lengths and angles of the geometrical structures for 2D D-J $CsPbI_3$. (e) A schematic diagram of the interaction between the organic layer and the inorganic octahedron mediating carrier transport. (f) Charge densities of the VBM in PDA-Pb and F-PDA-Pb. (g) The band structures and density of states for F-PDA-Pb (n = 2–5), respectively. The Fermi level is set to zero. The CB, VB, CBM, and VBM are conduction band, valence band, conduction band minimum, and valence band minimum orbital.

In theory, the enhanced molecular polarity can increase the dielectric constant of organic spacer, thereby expanding the dielectric screening ability, rationalising effective carrier separation. However, in the process of actually forming 2D perovskites, the situation may be more complicated, because the dipole moment is directly related to the orientation of organic molecules. The influence on the properties of 2D perovskites also depends on further characterization with subsequent development [31,32]. In order to confirm it experimentally, we extract the exciton transition peak position and the onset of band-to-band absorption edge from the Tauc plot as shown in Fig. S1 (online). We find that the exciton transition peak appears at 2.33 eV for (F-PDA)PbI_4, and a linear fitting curve provides the onset of continuum at 2.47 eV, yielding an exciton binding energy of 140 meV. For the (PDA)PbI_4, exciton transition peak locates at 2.82 eV and the onset of continuum appears at 3.09 eV, yielding a much larger exciton binding energy of 270 meV. This shows that the fluorinated spaced cation does reduce the exciton binding energy, which is consistent with the simulation results.

Then, the organic spacer and its subtle interaction with adjacent inorganic layer have obvious influence on 2D perovskite structure when the organic spacer is inserted into the octahedron [33]. Fig. S2 (online) shows the 2D D-J structure with n = 4 optimized by DFT, representing (F-PDA)$Cs_3Pb_4I_{13}$ (shorthand for F-PDA-Pb) and (PDA)$Cs_3Pb_4I_{13}$ (shorthand for PDA-Pb), respectively. We noticed that the 2D D-J $CsPbI_3$ structure was not disrupted by the fluorinated spacer in terms of macroscopic structure. Structurally, as shown in Fig. 1b, the two H atoms on the amine group head of the organic cation are hydrogen-bonded with terminal I atoms of the octahedron, and the other H atom is connected with I atoms of second nearest neighbored octahedron layer, thereby stabilizing the 2D system [34]. In detail, the ordered structure is stabilized by the strong electrostatic attraction between the organic and inorganic components, and this effect is measured by the distance between N and I. The average N···I distance of the corresponding 2D perovskite structure is given in Fig. S3a (online), where the stronger hydrogen bonding in the F-PDA-Pb component means that the organic cations are more significantly coupled to the $[PbI_6]^{4-}$ planes. As reported, this is because the highly electronegative fluorine atoms inductively withdraw electron density out of the aromatic ring and leaving a rich positive charge at the $-NH_3^+$ group, resulting in a stronger electrostatic interaction between $-NH_3^+$ in F-PDA and I in corner-sharing $[PbI_6]^{4-}$ layers [35]. Concurrently, this strong NH···I interaction partially suppresses the thermal fluctuation of the equatorial iodide, which is essential for the energy transfer between the organic cation and the $[PbI_6]^{4-}$ planes [36].

Molecular interactions in 2D structures are critical to determining and tuning desired physical properties. In the F-PDA spacer, the intermolecular and intramolecular CH···F distances are 2.3 and 2.62 Å (shorter than their van der Waals radii), respectively, indicating the existence of CH···F interactions [37]. The similar effects also exist between NH···F (Fig. 1c). These strong interactions induce an orderly distribution of spacers and increase the barrier of molecular motion in the final bulk [38]. Simultaneously, axial and equatorial Pb–I–Pb angles and Pb–I bond length qualitative reflect the distortion degree of inorganic octahedron, as shown in Fig. 1d and Fig. S3b–d (online), manifesting that H/F substitution is accompanied by enhanced coupling between spacer and inorganic layer [39]. In addition, the disturbance to the 2D perovskite structure caused by this is negligible.

Carrier transfer in 2D perovskites intrinsically depends on tunneling in organic interlayers, and thus there are several possible carrier transfer pathways: (1) interlayer coupling determined by

adjacent inorganic planes; (2) hydrogen bond and other non-covalent bond dominated by the interaction between spacer and inorganic octahedron; (3) carrier tunneling appeared within the organic spacer (Fig. 1e). Therefore, we can reasonably speculate that the (F-PDA)$Cs_{n-1}Pb_nI_{3n+1}$ structure could reduce the charge transfer barrier between $[PbI_6]^{4-}$ plane and bulk organic cations. Because in the above structural analysis, we have shown that the (F-PDA)$Cs_{n-1}Pb_nI_{3n+1}$ component has stronger hydrogen bonds and more other non-covalent interactions (such as CH···F and NH···F interactions) than (F-PDA)$Cs_{n-1}Pb_nI_{3n+1}$. To further confirm this hypothesis, we compared charge densities based on F-PDA-Pb and PDA-Pb components (n = 4) (Fig. 1f and Fig. S3 online). It was found that the $[PbI_6]^{4-}$ octahedron near the organic cation layer emerged enrich charge accumulation in valence band maximum (VBM) for F-PDA-Pb compared with PDA-Pb components. This result indicates that the F-PDA-Pb component has superior charge transfer properties between the spacer layer and the inorganic layer, which is consistent with the results discussed above [23].

As shown in Fig. 1g and Fig. S4 (online), the DFT electronic structure calculations are correspondingly deployed, which reveals the hybridization of Pb s and I p orbitals in VB and dominated Pb p orbitals in CB [22]. The band gap variation with the number of layers is expected, which is the effect of organic cations on the tuning of the octahedral structure. Further, we compared the partial density of states (pDOS) of the organic components, and observed the F-PDA-Pb pDOS of the structures with fluorine functional group which are closer to the band edges in the CB than PDA-Pb components (Fig. S6 online). This simply reflects that C–C $\pi(\pi^*)$ orbitals in the F-PDA ligands are less stabilized (destabilized) than the PDA ligands, and thus also contribute to a better carrier mobility between the organic and inorganic layers induced by the F-PDA ligands [40]. The above results indicate that the tailoring of the organic cation structure improves the coupling between the spacer and the inorganic layer and dramatically affects the charge transport there, which motivates us to further explore the crystallization, charge transfer kinetics and photovoltaic performance of 2D D-J $CsPbI_3$ perovskites with different spacer structures.

To experimentally determine the formed 2D D-J structure, we tested X-ray diffraction (XRD) of (F-PDA)PbI_4 and (PDA)PbI_4 films, respectively, and compared them with typical R-P type structures $(BA)_2PbI_4$. As shown in Fig. S7 (online), the diffraction pattern exhibits peak at low diffraction angle (2θ = 10.85°, 8.83° and 6.40°, respectively), corresponding to interplanar d-spacing of 8.138, 9.942, and 12.396 Å, respectively, which provides a fingerprint of the layered structure. It can be seen that the d-spacing in the R-P structure is significantly increased, which is the result of the alternating arrangement of the two layers of spaced cations between the inorganic octahedrons. Further, we note that PDA-derived spacers do form a 1D structure in previous reports [41]. In fact, Wu and co-workers [23] and Yip and co-workers [42] believe that the PDA can also form 2D structures in recent reports. In order to clarify this point more clearly, we analyzed the (PDA)PbI_4 structure through theoretical calculations and found that it is a 2D structure with $[PbI_6]^{4-}$ octahedral and organic components alternately arranged (Fig. S8a online). On this basis, the morphology characteristics were further analyzed, which is mainly characterized by a typical 2D layered structure (Fig. S8b online). Meanwhile, we prepared (PDA)PbI_4 single crystals, which can be clearly seen in the form of flake growth, which is a typical feature of 2D perovskites (Fig. S8c online). Therefore, we consider the (PDA)PbI_4 structure as a whole to behave as a 2D structure. Of course, we acknowledge that a one-dimensional (1D) competing phase may be formed during the preparation of (PDA)PbI_4, which may be related to the preparation conditions, that is, the difference of crystallization process between the two, which is difficult to be clearly characterized in the experiment.

Finally, the 2D D-J $CsPbI_3$ (n = 4) crystal structure and orientation were examined. All the films showed two main diffraction peaks around 14.1° and 28.3°, corresponding to the (111) and (202) diffraction planes, respectively. The slight shifted diffraction peak to higher angle indicates that fluorine-substituted F-PDA organic spacer cations cause lattice contraction. Based on the previous discussion, we speculate that this is due to the stronger interaction between organic spacer and inorganic plane, which leads to a slight contraction of the lattice and a decrease in the spacing between the crystal planes [43]. Notably, the diffraction intensity ratio of (202)/(111) of F-PDA-Pb increased from 0.67 to 0.97 compared with PDA-Pb, indicating that the layered 2D phase tends to grow perpendicular to substrate, which is more conducive to carrier transport along the out-of-plane direction (Fig. 2b).

In order to experimentally reveal the H/F substitution of spacers and the deduction of 2D D-J $CsPbI_3$ behavior, we selected F-PDA-Pb and PDA-Pb component for in-depth exploration. We performed Fourier transform infrared (FTIR) spectroscopy characterization to explore the interlayer electrostatic interaction in F-$PDAI_2$, $PDAI_2$ powder, F-PDA-Pb, and PDA-Pb samples. The F-$PDAI_2$ powder presents a peak at 1235 cm^{-1} which corresponding to the C–F bond stretching vibration. As expected, this peak was absent in the $PDAI_2$ sample (Fig. S9a online). However, the fingerprint peak of C–F bonds was shifted to lower wavenumber (1218 cm^{-1}) in F-PDA-Pb films sample, which illustrates that the electron-deficient F atoms engender interaction with electron-rich benzene rings (Fig. 2a) [44]. This is in line with our simulation results.

To evaluate the optical properties of 2D D-J $CsPbI_3$ films prepared with different spacers, steady-state absorption and photoluminescence (PL) spectra were further tested. As shown in Fig. 2c, F-PDA-Pb and PDA-Pb film exhibits multiple excitonic absorption peaks, corresponding to low-n phases (n = 1, 2, 3), and a low absorption band related to 3D-like phases. Combined with the absorption characteristics of the pure phase n = 1, the exciton peak of F-PDA-Pb (n = 1) sample appears red-shift compared to PDA-Pb (n = 1), which can be attributed to the increase of the dielectric constant of the spacer cation, thus weakening the quantum constraint effect [45]. For all 2D D-J $CsPbI_3$, the PL is dominated by the emission from the 3D-like phases. Consistent with the absorption spectra, this PL emission peak shows red-shift upon for F-PDA-Pb (Fig. S9b online). It is worth noting that the corresponding small n-phase exciton peak does not appear in the PL spectrum. This is due to the fact that in the 2D perovskite phase with n = 4 as the main bulk, there are fewer other low-dimensional phases. Therefore, when using 365 nm laser excitation, the faint light emitted by the small n phase is absorbed by the 2D phase adjacent to the larger n value, that is, the self-absorption effect occurs. Thus the whole spectrum shows the appearance of a 3D-like emission peak. Similar phenomena have been reported in previous literatures [19,46].

Next, the scanning electron microscope (SEM) and top-view atomic force microscopy (AFM) investigated the surface morphology of the 2D D-J $CsPbI_3$ film. During the insertion of abundant organic components into 3D $CsPbI_3$, 2D counterpart presents inherent crystallization difficulties due to steric hindrance effects of bulk organic cations that restrict grain growth in specific directions. Therefore, the PDA-Pb film shows obvious cracks and pinholes, as well as worse disordered grain orientation and larger surface roughness. Unexpectedly, F-PDA-Pb film exhibits denser, smoother morphology, and desired grain orientation (Fig. 2d, e). It is worth noting that the mechanism behind the more optimized morphology of F-PDA-Pb films is not very clear. We speculate that F-PDA molecules with high polarity have higher electron-donor capabilities than PDA, making it easier to coordinate with electron-acceptor Pb^{2+}. That is, they can compensate for the crys-

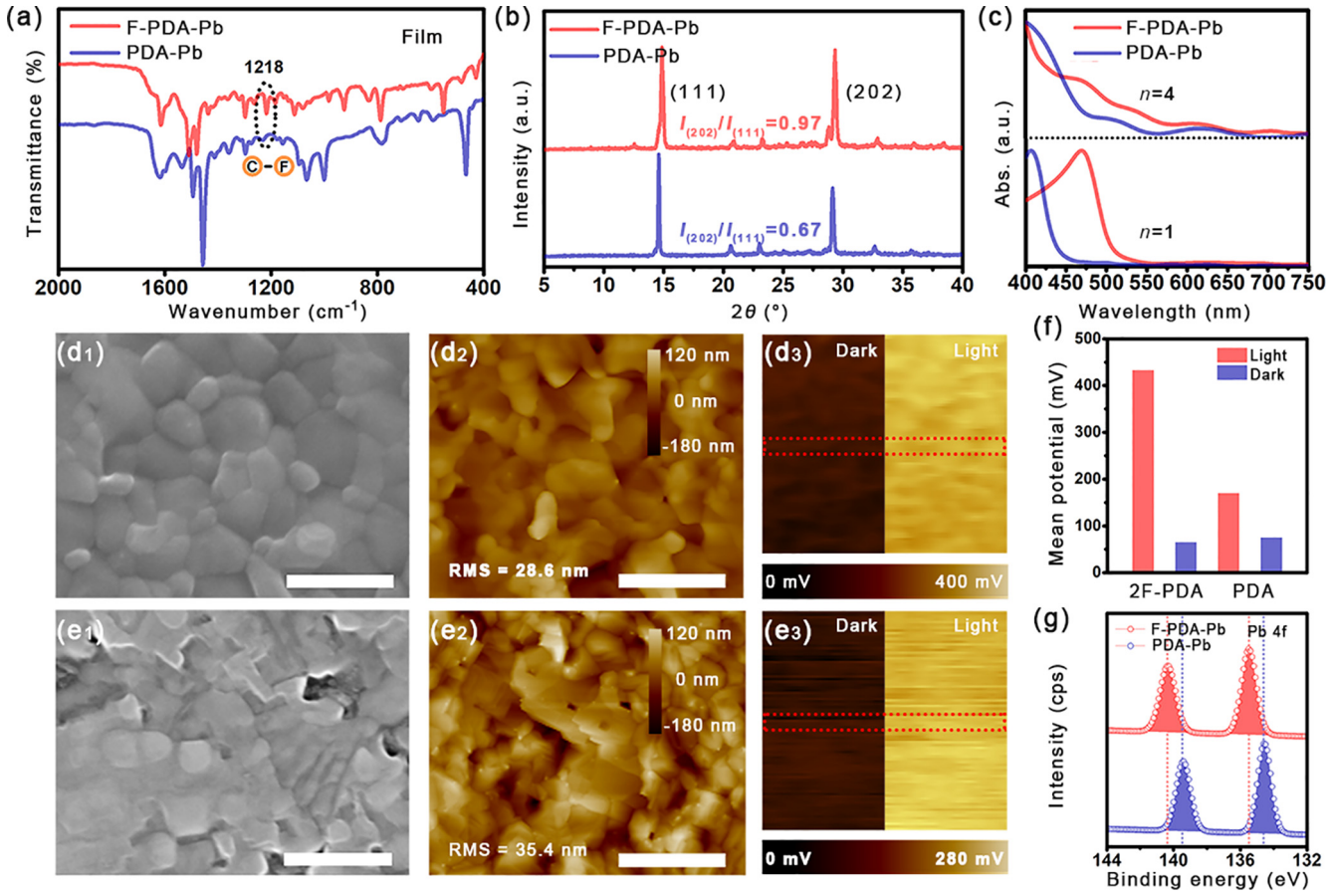

Fig. 2. (Color online) Characterizations of PDA-Pb and F-PDA-Pb film. (a) FTIR spectrometer spectra; (b) XRD patterns; (c) UV–vis absorption spectra of 2D $CsPbI_3$ (n = 1 and n = 4). SEM images for F-PDA-Pb film (d_1) and PDA-Pb film (e_1), top-view AFM for F-PDA-Pb film (d_2) and PDA-Pb film (e_2), and surface potential under dark and light condition for F-PDA-Pb film (d_3) and PDA-Pb film (e_3), respectively. RMS is short for root-mean-square. Scale bar, 2 μm. (f) Corresponding mean potential values (CPS, count per second) and (g) X-ray photoelectron spectroscopy spectra of Pb 4f.

tallization difficulties caused by the steric hindrance of organic cations, resulting in higher quality 2D perovskite film [47].

Further, the scanning Kelvin probe microscopy (SKPM) with and without illumination is adopted to analyze the surface potential difference (ΔV) for F-PDA-Pb and PDA-Pb films. The potential of PDA-Pb film increases from ~60 meV to a higher value of ~120 meV (ΔV = 60 meV), instead, the F-PDA-Pb film shows a dramatic fluctuation (~50 to ~440 meV, ΔV = 390 meV) (Fig. 2f). It can be clearly seen that they have similar surface potential in the dark, while there is a larger surface potential in F-PDA-Pb film in the light soaking. We know that the surface potential reflects carrier concentration in the surface region, which means that more carriers can move to the surface region when lighting in F-PDA-Pb film. This is a more obvious manifestation of light response. In addition, Cao and co-workers [48] reported that although ΔV cannot be directly converted into V_{OC}, it is closely related to the intensity of photovoltaic effect. Because a larger surface potential can provide appropriate band bending, which is conducive to hole extraction. This is also consistent with our experimental results.

We estimated the effect of organic cationic structure on octahedral interactions with X-ray photoelectron spectroscopy (XPS) testing. In compared with PDA-Pb, the Pb 4f and I 3d peaks shift to higher binding energy in F-PDA-Pb films (Fig. 2g and Fig. S9c online). For Pb 4f, this is caused by electrostatic interaction between fluorine atoms in F-PDA spacer and $[PbI_6]^{4-}$ octahedron. For I 3d, this is the formation of the stronger NH–I hydrogen bonds and more other non-covalent interactions, such as CH···F and NH···F [49]. In conclusion, we have experimentally demonstrated series of conclusions of the above structural simulation part. In addition, these bondings also have a significant regulatory effect on the crystallization quality of the 2D perovskite film, as we discussed in the SEM section. Subsequently, the energy levels of the two 2D D-J $CsPbI_3$ films were measured by ultraviolet photoelectron spectroscopy (UPS) (Fig. S10a, b online). Compared with the PDA-Pb, the CB of the F-PDA-Pb film was changed from −3.49 to −3.64 eV. The schematic diagram for the energy levels of the 2D D-J $CsPbI_3$ is constructed and shown in Fig. S10c (online). It is evident that the F-PDA-Pb film has the most compatible energy level alignments to those of the selected electron/hole transport layers.

In order to ascertain the spatial phase distribution and charge transfer kinetics in the 2D D-J $CsPbI_3$ film, we performed ultrafast transient absorption (TA) spectroscopy measurements. Fig. 3a, b represent the 2D TA contour map of the 2D D-J $CsPbI_3$ excited from the back side. The F-PDA-Pb and PDA-Pb films all show the ground state bleaching (GSB) signal of 2D (or mixed low-n phase) and 3D-like phase. Fig. 3c, d show the time-dependent TA spectra of each film. Upon excitation, at early stage (≤0.3 ps), we observed a bleach signal of small n phases (n = 2) and bleach signal from large n components in the case of F-PDA-Pb and PDA-Pb films. As time evolves, the relative GSB peak intensity of the low-n phase relative to the 3D-like phase gradually decreases, indicating an efficient cascade energy transfer from the low-n phase to the 3D-like phase [50].

Moreover, the dynamic process of charge transfer was further presented. The kinetics of each PB can be fitted by a multiexponential function: $\Delta A(t) = a_1\exp(-t/\tau_1) + a_2\exp(-t/\tau_2) + a_3\exp(-t/\tau_3)$

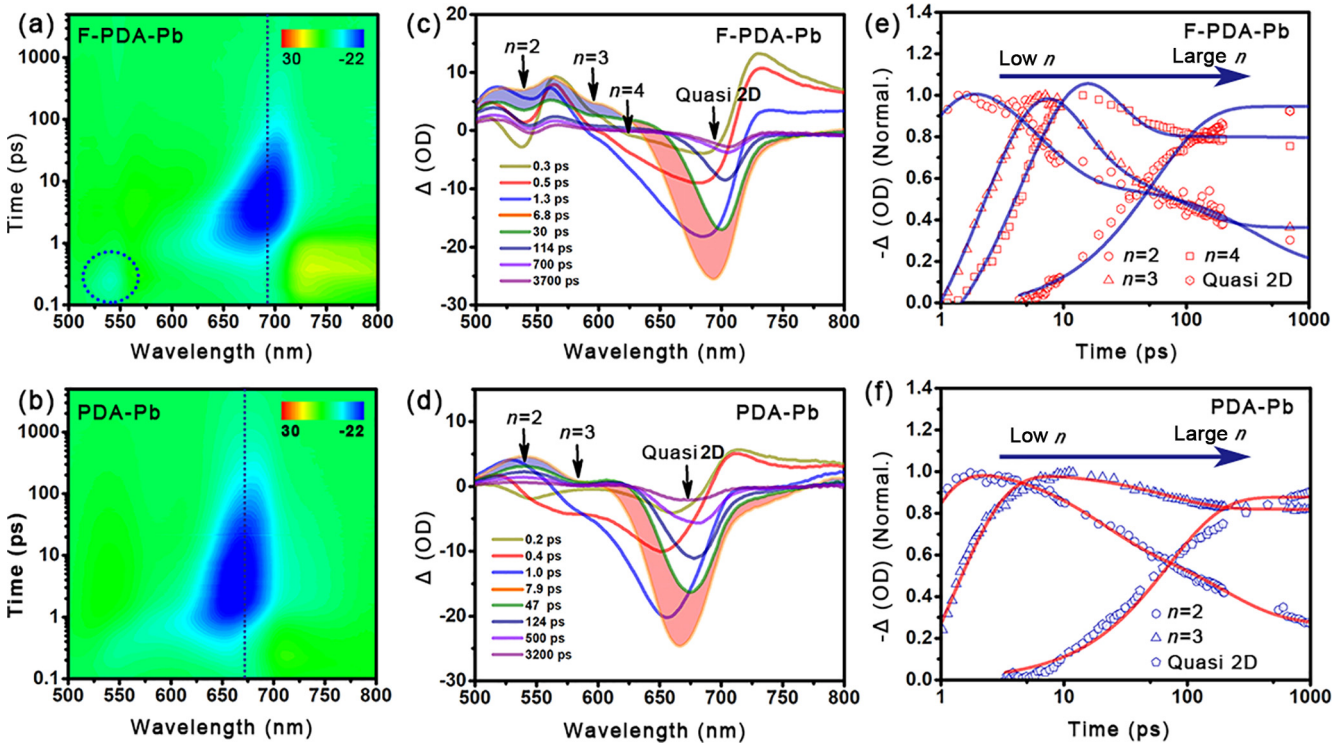

Fig. 3. (Color online) TA spectra. Time- and wavelength-dependent TA images, TA spectra at selected probe times and TA spectra of different *n* phases as a function of delay time for (a, c, e) F-PDA-Pb film and (b, d, f) PDA-Pb film, respectively. OD stands for optical density.

$- c_1\exp(-t/\tau_{et})$, where a_1, a_2, a_3, and c_1 are amplitudes; τ_1 is the fast decay time constant due to the carrier transfer process in the perovskite; τ_2 and τ_3 represent the slow decay time constant; and τ_{et} is the formation time constant. The low-*n* phases of n = 2, 3, and 4 in F-PDA-Pb film exhibit ultrafast decay time of τ_1 = 0.26, 0.46, and 13.2 ps, respectively. Whereas, PDA-Pb analogue shows longer times of τ_1 = 0.32 and 18.57 ps for the phases of n = 2 and 4, respectively. In unison, the rising time of F-PDA-Pb and PDA-Pb from the low-*n* phase to the 3D-like phase are also extracted, which are 23.1 and 131 ps, respectively (Fig. 3e, f). We attribute this more efficient energy transfer in F-PDA-Pb to three aspects: First, the F-PDA^{2+} with high dipole moment impels the 2D D-J $CsPbI_3$ system dielectric constant to increase, which makes the excitons more easily dissociated. Second, fluorine substitution in the organic layer also affects intermolecular stacking and electron interaction, which makes the coupling between excitons and lattice more obvious and thus energy transmission more favorable. Finally, the 2D perovskite phases tend to grow vertically, and thus the spatially uniform and orderly distributed energy landscape minimize the out-of-plane charge transport resistance caused by insulating organic cations in the F-PDA-Pb samples (Fig. S11 online) [43,51].

To reveal the effects of two organic spacers on the photovoltaic performance of 2D D-J $CsPbI_3$ devices, we prepared typical n-i-p solar cells with FTO/TiO_2/perovskite/Spiro-OMeTAD/Au conformation (Fig. 4a). Fig. 4a, Fig. S12a (online) and Table 1 show the current density-voltage (*J-V*) curves of the champion F-PDA-Pb and PDA-Pb devices under AM 1.5 G illumination in reverse and forward scan direction. The reference PDA-Pb based device obtained a PCE of 12.4%, in contrast, the overall parameters of the F-PDA-Pb based sample have been improved, resulting in a remarkable high PCE of 15.12%. To the best of our knowledge, this PCE value is among the highest efficiency for the reported 2D D-J $CsPbI_3$ PSCs with $n \leq 5$. The integrated J_{SC} of F-PDA-Pb PSCs obtained from the external quantum efficiency (EQE) is shown in Fig. 4b, which closely matched with the measured J_{SC}. Notably, the distinguished efficiency of the F-PDA-Pb PSCs was further proved by the steady state PCE of 14.9% measured at the maximum power point (0.91 V) nearly 300 s (Fig. 4c).

Additionally, 20 independent samples were prepared to evaluate the repeatability of device performance. As shown in Fig. 4d and Fig. S12b–d (online), the F-PDA-Pb PSCs show better photovoltaics performance and repeatability. Mott-Schottky analysis was further used to investigate the built-in potentials (V_{bi}) difference for reference and optimized film as Fig. 4e. The larger V_{bi} in the F-PDA-Pb samples can enhance the driving force for carrier injection at the interface [52]. We then evaluated the stability of unencapsulated devices under conditions of ~40% relative humidity. As shown in Fig. 4f, the 3D $CsPbI_3$ maintains 70% of the initial PCE after 300 h, while the PCEs of the 2D PDA-Pb and F-PDA-Pb devices drop to about 80% and 90% under the same circumstances, respectively. Meanwhile, we performed the contact angles of three kinds of perovskite films (3D, PDA-Pb and F-PDA-Pb), which were 30°, 52°, and 72° respectively. On the whole, 2D films are more hydrophobic, while F-PDA-Pb is the most hydrophobic (Fig. S13 online). The improvement of the overall humidity stability is mainly attributed to the hydrophobic effect of the organic spacer cations in the bulk and the surface of the 2D D-J $CsPbI_3$ films [53]. Especially for F-PDA-Pb samples, the diffusion channels of water molecules are further compressed structurally due to the stronger hydrophobicity of fluorine atoms and the stronger significant interaction between organic cations and inorganic octahedrons in this component [54]. It should be mentioned that the degradation of device performance is also related to the failure of the buffer layer and the electrode. In particular, the material used in the hole transport layer, that is, the doped Spiro-OMeTAD, is sensitive to humidity conditions.

Finally, we have made statistics on the performance of the 2D D-J $CsPbI_3$ ($n \leq 5$) devices recently reported, mainly based on the R-P and D-J type structures caused by common monoamines and diami-

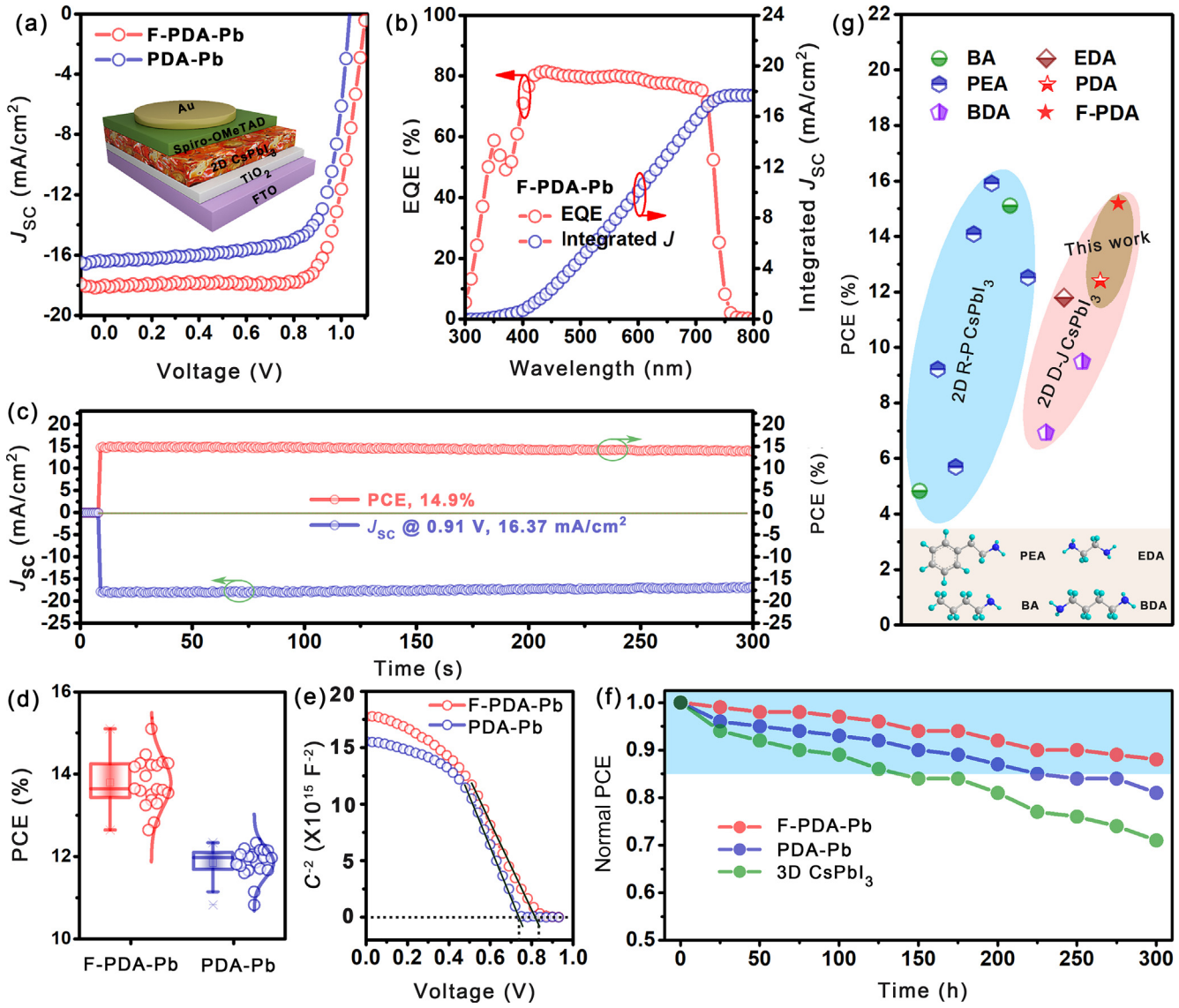

Fig. 4. (Color online) Photovoltaic performance and stability characterization. (a) Reverse scan *J-V* curve. (b) EQE spectra of the F-PDA-Pb PSCs. (c) Stabilized power output and current density of the F-PDA-Pb PSCs. (d) PCE distribution (20 individual devices were collected). (e) Mott-Schottky curves. (f) Stability test of unencapsulated 3D $CsPbI_3$ and 2D D-J $CsPbI_3$ PSCs in an atmospheric environment with a humidity of 40%. (g) Record PCE of 2D D-J/R-P $CsPbI_3$ (nominal $n \leq 5$) PSCs relative to reported work.

Table 1
J-V parameters of the $(PDA)Cs_3Pb_4I_{10}$ and $(F\text{-}PDA)Cs_3Pb_4I_{10}$ PSCs under forward and reverse scan directions extracted from Fig. 4a and Fig. S9a (online). FF, fill factor.

Films	Scan mode	V_{OC} (V)	J_{SC} (mA/cm^2)	FF (%)	PCE (%)
$(PDA)Pb_3Cs_4I_{13}$	Reverse	1.03	16.42	72.95	12.41
	Forward	0.92	16.74	74.55	11.47
$(F\text{-}PDA)Pb_3Cs_4I_{13}$	Reverse	1.10	17.99	76.17	15.12
	Forward	1.08	17.87	75.46	14.59

nes (all devices have an effective area of 0.09 cm^2) (Fig. 4g). Compared with the previously reported 2D D-J $CsPbI_3$ devices, our optimized devices achieved the best performance due to rational design of organic components and efficient regulation of 2D intrinsic structures. To purely explore the effect of organic spacers on the 2D structure, our experiments avoid further modification of the corresponding devices. From this point of view, our 2D D-J $CsPbI_3$ device performance is also a breakthrough compared to the control device of R-P counterparts reported by Yao et al. [5] (the PCE of the reference $(PEA)_2Cs_3Pb_4I_{13}$ device is 12%). Essentially, it is due to the unique structural contribution of the D-J phase.

From the above series of analysis, we can find that the performance of F-PDA-Pb superior to that of PDA-Pb devices. Therefore, we elaborated exploration and comparison to the interior nature of the two kind devices to further unravelling the structure-performance relationship of 2D D-J $CsPbI_3$. The dissociation of excitons and charges transport within the device directly reflect the photophysical properties. Here we measured the photocurrent density versus effective voltage (J_{ph}-V_{eff}) to determine this feature. As shown in Fig. 5a, J_{ph} increases with the increase of V_{eff} and reaches saturation state to a certain extent, which means there is enough built-in electric field to separate all of charges to the corre-

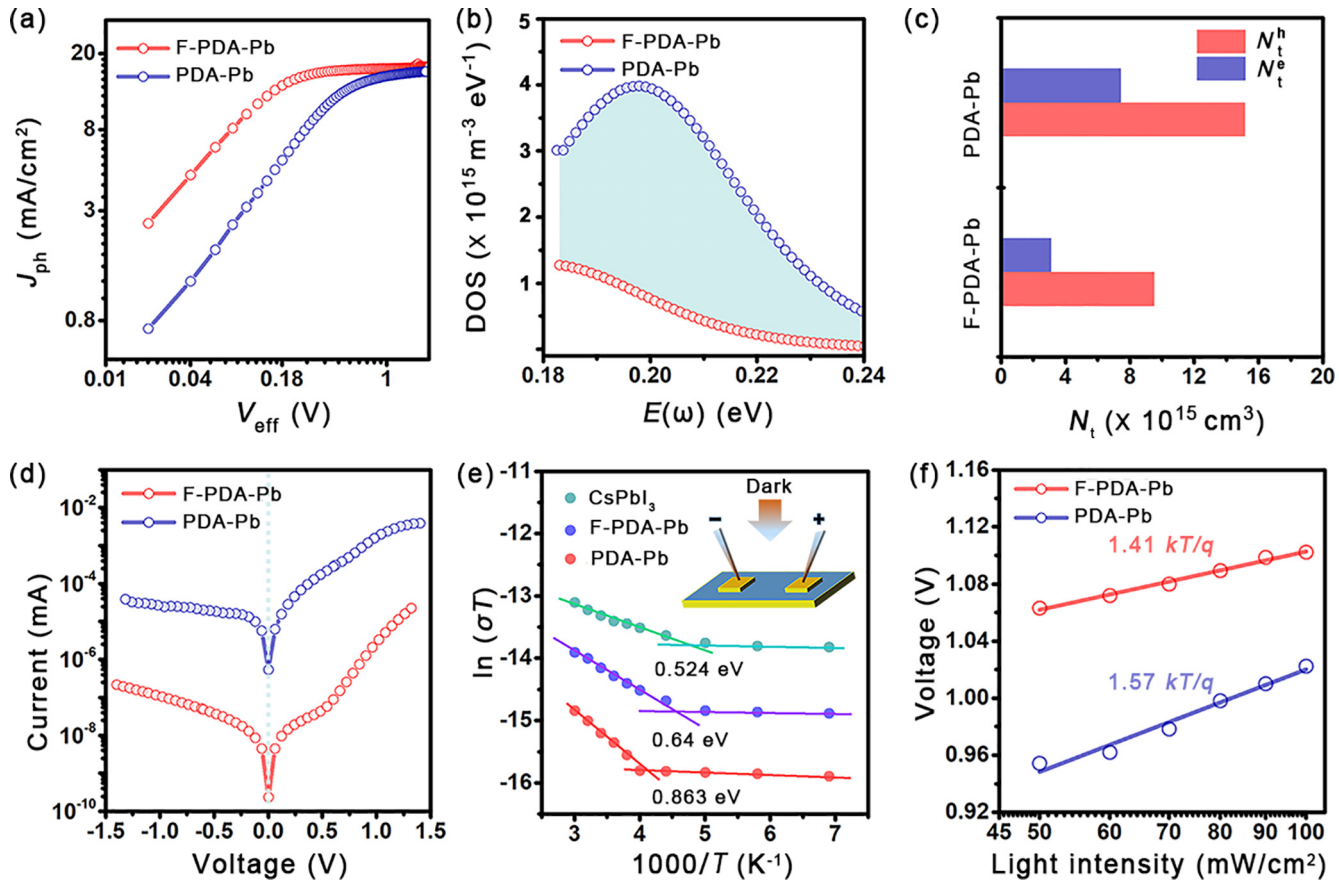

Fig. 5. (Color online) Electrical characteristics of F-PDA-Pb and F-PDA-Pb based devices. (a) Photocurrent density versus effective voltage (J_{ph}-V_{eff}) on a double-logarithmic scale. J_{ph} is defined as the difference between photocurrent density and dark current density (the photocurrent test is consistent with the above); V_{eff} represents the difference between the voltage when J_{ph} is equal to zero and the applied bias voltage. (b) The trap state density at room temperature. (c) Trap density; (d) dark *J*-*V* curves; (e) temperature-dependent conductivity; (f) seminatural logarithmic plots of V_{OC} versus light intensity.

sponding electrode. Under short-circuit conditions and maximum power output conditions, the J_{ph}/J_{sat} ratio calculated by F-PDA-Pb and PDA-Pb are 0.964 (0.946) and 0.911 (0.862), respectively. A larger J_{ph}/J_{sat} ratio indicates a higher efficiency of exciton dissociation and charge collection in F-PDA-Pb PSCs [20].

We further quantified the defect state density in the 2D D-J $CsPbI_3$ film, and explored the related charge recombination behavior. As shown in Fig. 5b, we used the thermal admittance spectroscopy to depict the defects energy distribution in the film. The F-PDA-Pb sample exhibits the shallower defect density of states (tDOS) across the entire trap depth, the corresponding defect density is 1.3×10^{15} m^{-3} and the tDOS with an energy level above 0.18 eV. Yet, the defects in the PDA-Pb film are abundant (4×10^{15} m^{-3}) and even more deeply distributed (the tDOS with an energy level above 0.2 eV). This is consistent with the defect density trend extracted from the space charge limited current (SCLC) technology (Fig. 5c and Fig. S14 online) [55]. The carrier lifetime in the dynamics process are also extracted from time-resolved PL (TRPL) measurement, which can be fitted by a biexponential function of $I(t) = I_0 + a_1\exp(-t/\tau_1) + a_2\exp(-t/\tau_2)$, where a_1, a_2 are the amplitudes; τ_1, τ_2 represent time constants for fast and slow decay lifetimes (Fig. S15 online). The longer carrier lifetime in F-PDA-Pb confirms the availability of high-quality devices. The higher carrier diffusion length in F-PDA-Pb confirms the availability of high-quality devices. Fig. 5e shows the dark *J*-*V* curves. The F-PDA-Pb PSC shows smaller leakage current than the PDA-Pb based device, which is due to the improvement of film quality and reduction of defect quantity [56].

Ion migration in metal halide perovskites is considered to be the origin of structural instability as well as the inducement of some unwanted optoelectronic phenomena, such as hysteresis effect. It is usually dominated by the weak bonding of the perovskite structure and its intrinsic defects [57]. Here, we measured the activation energy (E_a) for ion migration in perovskite films with temperature-dependent electrical conductivity in dark. Briefly, we used a laterally structured device consisting of two Au electrodes deposited on perovskite film, as shown in Fig. 5f. It should be noted that the lateral device structure is adopted here to suppress the electronic conduction, thereby highlighting the contribution of ionic conduction to the total current. The E_a can be extracted from the Nernst-Einstein relation: $\sigma(T) = (\sigma_0/T)\exp(-E_a/k_BT)$, where k_B is the Boltzmann constant, σ_0 is a constant, and T is temperature [58]. For all three perovskite films, we observed a transition from electronic to ionic conductivity with decreasing temperature. Among them, the E_a of the extracted 3D $CsPbI_3$ film is 0.524 eV, while the E_a of the PDA-Pb and F-PDA-Pb films are 0.64 and 0.863 eV, respectively. We thus conclude that: (1) the insertion of insulating organic cations in 2D D-J $CsPbI_3$ blocks the path of ion migration, making it difficult to move within the perovskite bulk, as shown in Fig. S16 (online). (2) For 2D F-PDA-Pb film, the ionic binding energy is enhanced by the stronger hydrogen bond and more other non-covalent bond (such as CH···F and NH···F interactions) between inorganic layer and organic spacer, thus increasing the ion migration energy. Moreover, the efficient manipulation of film quality results in less defect films, which is the fundamental reason for ion migration control.

With that, we carry out a series of electrical characterization to analyze the carrier recombination in the device. The transient voltage decay (TPV) results in Fig. S17a (online) show that the F-PDA-Pb device has a slower photovoltage decay, indicating suppressed non-radiative recombination. The variation of V_{OC} dependent light intensity reflects the defect recombination mechanism dominated by SRH, and studies have shown that the ideality factor of a perfect device is closer to 1 [59]. As shown in Fig. 5f and Fig. S17b (online), the ideality factor of F-PDA-Pb PSCs reduced from $1.57k_BT/q$ to $1.41k_BT/q$ compared to that of the PDA-Pb PSCs (T: temperature, and q: elementary charge), which indicates drastically reduced defect-assisted recombination under device operating conditions. To further verify the charge transfer and recombination behavior at the 2D D-J $CsPbI_3$ interface with different spacers, the test of electrochemical impedance spectroscopy (EIS) in the dark state is adopted in the Fig. S18 (online). The recombination resistance (R_{rec}) and capacitance (C_{rec}) are obtained by fitting the Equivalent circuit. The F-PDA-Pb PSCs possesses a larger R_{rec} than PDA-Pb PSCs, which indicates that the charge transfer was promoted and the charge recombination was restrained in the F-PDA-Pb samples [60].

In connection with theoretical analysis, the superior photovoltaic performance of F-PDA-Pb devices is mainly dominated by the intrinsic microstructure. Significantly, the stronger intermolecular interaction between the fluorinated organic spacer and the octahedron mediates the self-assembly process of the crystal and obtains high-quality light-absorbing film, which is the crux to reducing defect states. Moreover, from the structural level, the strong bonding interaction (hydrogen bonds and other non-covalent bonds) of spacers promotes preferred molecule stacking in the organic and inorganic phase. Therefore, the energy barriers of $[PbI_6]^{4-}$ plane and bulk organic cations are weakened, and the unhindered passage of charge carriers is ensured.

4. Conclusion

To conclude, we have proved exceedingly efficient 2D D-J $CsPbI_3$ photovoltaic devices with outstanding stability by fine-tuning the organic spacer. By designing the spacer structure, the increase of the organic cation dipole moment weakens the screening of the space charge, which is conducive to the exciton dissociation. With the DFT simulation guidance, we informed that H/F substitution can maintain the symmetry of the crystal while reducing structural distortion and unexpected structural disorder. Concurrently, fluorinated spacers play an important role in the intermolecular interactions and constructions. The coupling between inorganic plane and organic chain is improved, and the carrier transport path is optimized, thus the potential barrier hindering the energy transport between them is alleviated. Consequently, F-PDA-Pb PSCs exhibit a champion PCE of 15.12%, which is among the highest efficiencies for 2D D-J $CsPbI_3$ ($n \leq 5$) PSCs to the best of our knowledge. The dramatically improved storage stability was realized with retaining an average 90% of their initial efficiency after 300 h. This study shows that the structural tailoring of fluorinated spacers has positive practical significance for the development of efficient and stable 2D D-J $CsPbI_3$ PSCs.

Conflict of interest

The authors declare that they have no conflict of interest.

Acknowledgments

This work was supported by the National Natural Science Foundation of China (52073131, 51902148, and 12047501), and the Fundamental Research Funds for the Central Universities (lzujbky-2021-it31, lzujbky-2021-59, lzujbky-2021-ct15, lzujbky-2021-ct01, and lzujbky-2021-sp69). The calculation work was supported by Supercomputing Center of Lanzhou University.

Author contributions

Yutian Lei and Zhiwen Jin performed the experiments, data analysis, and experimental planning. Zhen-Hua Li performed all theoretical studies and explanations. Haoxu Wang and Qian Wang helped perfect the experimental ideas. Haihua Zhang conducted the TAS test. Gang Wang was in charge of the AFM and SKPFM tests. Guoqiang Peng and Liming Ding provided guidance on the design and test of some electrical characterizations. The manuscript was written by Yutian Lei and Zhiwen Jin. All the authors reviewed the manuscript.

Appendix A. Supplementary materials

Supplementary materials to this article can be found online at https://doi.org/10.1016/j.scib.2022.05.019.

References

[1] Wang X, Wang Y, Chen Y, et al. Efficient and stable $CsPbI_3$ inorganic perovskite photovoltaics enabled by crystal secondary growth. Adv Mater 2021;33:e2103688.
[2] Li X, Hoffman JM, Kanatzidis MG. The 2D halide perovskite rulebook: how the spacer influences everything from the structure to optoelectronic device efficiency. Chem Rev 2021;121:2230–91.
[3] Gong J, Hao M, Zhang Y, et al. Layered 2D halide perovskites beyond Ruddlesden-Popper phase: tailored interlayer chemistries for high-performance solar cells. Angew Chem Int Ed 2021;61:e202112022.
[4] Zhang J, Hodes G, Jin Z, et al. All-inorganic $CsPbX_3$ perovskite solar cells: progress and prospects. Angew Chem Int Ed 2019;58:15596–618.
[5] Yao H, Peng G, Li Z, et al. Fine coverage and uniform phase distribution in 2D $(PEA)_2Cs_3Pb_4I_{13}$ solar cells with a record efficiency beyond 15%. Nano Energy 2022;92:106790.
[6] Fu P, Liu Y, Yu S, et al. Dion-Jacobson and Ruddlesden-Popper double-phase 2D perovskites for solar cells. Nano Energy 2021;88:106249.
[7] Xu Z, Lu D, Dong X, et al. Highly efficient and stable Dion-Jacobson perovskite solar cells enabled by extended pi-conjugation of organic spacer. Adv Mater 2021;33:e2105083.
[8] Ngai KH, Wei Q, Chen Z, et al. Enhanced electrochemical stability by alkyldiammonium in Dion-Jacobson perovskite toward ultrastable light-emitting diodes. Adv Opt Mater 2021;9:2100243.
[9] Zhang T, Dar MI, Li G, et al. Bication lead iodide 2D perovskite component to stabilize inorganic α-$CsPbI_3$ perovskite phase for high-efficiency solar cells. Sci Adv 2017;3:e1700841.
[10] Zhou Z, Yang S, Xu K, et al. Diammonium-cesium lead halide perovskite with phase-segregated interpenetrating morphology for photovoltaics. J Phys Chem Lett 2020;11:747–54.
[11] Fang Z, Shang M, Zheng Y, et al. Organic intercalation engineering of quasi-2D Dion-Jacobson α- $CsPbI_3$ perovskites. Mater Horiz 2020;7:1042–50.
[12] Mishra A, Ahlawat P, Fish GC, et al. Naphthalenediimide/formamidinium-based low-dimensional perovskites. Chem Mater 2021;33:6412–20.
[13] Su R, Xu Z, Wu J, et al. Dielectric screening in perovskite photovoltaics. Nat Commun 2021;12:2479.
[14] Li Z, Zhou F, Yao H, et al. Halide perovskites for high-performance X-ray detector. Mater Today 2021;48:155–75.
[15] Xiao B, Sun Q, Wang F, et al. Towards superior X-ray detection performance of two-dimensional halide perovskite crystals by adjusting anisotropic transport behavior. J Mater Chem A 2021;9:13209–19.
[16] Zhang F, Park So Y, Yao C, et al. Metastable Dion-Jacobson 2D structure enables efficient and stable perovskite solar cells. Science 2021;375:71–6.
[17] Cheng Y, Ding L. Perovskite/Si tandem solar cells: fundamentals, advances, challenges, and novel applications. SusMat 2021;1:324–44.
[18] Zhang D, Fu Y, Zhan H, et al. Suppressing thermal quenching via defect passivation for efficient quasi-2D perovskite light-emitting diodes. Light Sci Appl 2022;11:69.
[19] Yu S, Abdellah M, Pullerits T, et al. Asymmetric spacer in Dion-Jacobson halide perovskites induces staggered alignment to direct out-of-plane carrier transport and enhances ambient stability simultaneously. Adv Funct Mater 2021;31:2104342.
[20] Lv G, Li L, Lu D, et al. Multiple-noncovalent-interaction-stabilized layered Dion-Jacobson perovskite for efficient solar cells. Nano Lett 2021;21:5788–97.
[21] Xie J, Yan K, Zhu H, et al. Identifying the functional groups effect on passivating perovskite solar cells. Sci Bull 2020;65:1726–34.

[22] Wang Z, Ganose Alex M, Niu C, et al. First-principles insights into tin-based two-dimensional hybrid halide perovskites for photovoltaics. J Mater Chem A 2018;6:5652–60.
[23] Fang Z, Hou X, Zheng Y, et al. First-principles optimization of out-of-plane charge transport in Dion-Jacobson $CsPbI_3$ perovskites with π-conjugated aromatic spacers. Adv Funct Mater 2021;31:2102330.
[24] Zhou Q, Liang L, Hu J, et al. High-performance perovskite solar cells with enhanced environmental stability based on a $(p\text{-}FC_6H_4C_2H_4NH_3)_2[PbI_4]$ capping layer. Adv Energy Mater 2019;9:1802595.
[25] Wang L, Zhou Q, Zhang Z, et al. A guide to use fluorinated aromatic bulky cations for stable and high-performance 2D/3D perovskite solar cells: the more fluorination the better? J Energy Chem 2022;64:179–89.
[26] Zhang H-Y, Zhang Z-X, Song X-J, et al. Two-dimensional hybrid perovskite ferroelectric induced by perfluorinated substitution. J Am Chem Soc 2020;142:20208–15.
[27] Zhou Q, Zuo C, Zhang Z, et al. F-containing cations improve the performance of perovskite solar cells. J Semicond 2022;43:010202.
[28] Zhang F, Kim DH, Lu H, et al. Enhanced charge transport in 2D perovskites via fluorination of organic cation. J Am Chem Soc 2019;141:5972–9.
[29] Rao W, Li M, You X, et al. The role of fluorine-substituted positions on the phase transition in organic-inorganic hybrid perovskite compounds. Inorg Chem 2021;60:14706–12.
[30] Zhou Q, Xiong Q, Zhang Z, et al. Fluoroaromatic cation-assisted planar junction perovskite solar cells with improved V_{oc} and stability: the role of fluorination position. Solar RRL 2020;4:2000107.
[31] Li Q, Dong Y, Lv G, et al. Fluorinated aromatic formamidinium spacers boost efficiency of layered Ruddlesden-Popper perovskite solar cells. ACS Energy Lett 2021;6:2072–80.
[32] Wang J, Liu Y, Han S, et al. Ultrasensitive polarized-light photodetectors based on 2D hybrid perovskite ferroelectric crystals with a low detection limit. Sci Bull 2021;66:158–63.
[33] Cheng L, Meng K, Qiao Z, et al. Tailoring interlayer spacers for efficient and stable formamidinium-based low-dimensional perovskite solar cells. Adv Mater 2021;34:e2106380.
[34] Li D, Xing Z, Huang L, et al. Spontaneous formation of upper gradient 2D structure for efficient and stable quasi-2D perovskites. Adv Mater 2021;33:e2101823.
[35] Abate A, Saliba M, Hollman DJ, et al. Supramolecular halogen bond passivation of organic–inorganic halide perovskite solar cells. Nano Lett 2014;14:3247–54.
[36] Ren Z, Yu J, Qin Z, et al. High-performance blue perovskite light-emitting diodes enabled by efficient energy transfer between coupled quasi-2D perovskite layers. Adv Mater 2021;33:e2005570.
[37] Mao L, Stoumpos CC, Kanatzidis MG. Two-dimensional hybrid halide perovskites: principles and promises. J Am Chem Soc 2019;141:1171–90.
[38] Cortecchia D, Neutzner S, Srimath Kandada A, et al. Broadband emission in two-dimensional hybrid perovskites: the role of structural deformation. J Am Chem Soc 2017;139:39–42.
[39] Fu X, He T, Zhang S, et al. Halogen-halogen bonds enable improved long-term operational stability of mixed-halide perovskite photovoltaics. Chem 2021;7:3131–43.
[40] Ni C, Huang Y, Zeng T, et al. Thiophene cation intercalation to improve band-edge integrity in reduced-dimensional perovskites. Angew Chem Int Ed 2020;59:13977–83.
[41] Ma C, Shen D, Huang B, et al. High performance low-dimensional perovskite solar cells based on a one dimensional lead iodide perovskite. J Mater Chem A 2019;7:8811–7.
[42] Niu T, Xue Q, Yip H-L. Advances in Dion-Jacobson phase two-dimensional metal halide perovskite solar cells. Nanophotonics 2020;10:2069–102.
[43] Shao M, Bie T, Yang L, et al. Over 21% efficiency stable 2D perovskite solar cells. Adv Mater 2022;34:e2107211.
[44] Zhang T, Nakajima T, Cao H, et al. Controlling quantum-well width distribution and crystal orientation in two-dimensional tin halide perovskites via a strong interlayer electrostatic interaction. ACS Appl Mater Interfaces 2021;13:49907–15.
[45] Wang H, Chan CCS, Chu M, et al. Interlayer cross-linked 2D perovskite solar cell with uniform phase distribution and increased exciton coupling. Solar RRL 2020;4:1900578.
[46] Li P, Liang C, Liu X-L, et al. Low-dimensional perovskites with diammonium and monoammonium alternant cations for high-performance photovoltaics. Adv Mater 2019;31:1901966.
[47] Liu C, Yang Y, Rakstys K, et al. Tuning structural isomers of phenylenediammonium to afford efficient and stable perovskite solar cells and modules. Nat Commun 2021;12:6349.
[48] Zhao Z, Chen X, Wu H, et al. Probing the photovoltage and photocurrent in perovskite solar cells with nanoscale resolution. Adv Funct Mater 2016;26:3048–58.
[49] Kan C, Tang Z, Yao Y, et al. Mitigating ion migration by polyethylene glycol-modified fullerene for perovskite solar cells with enhanced stability. ACS Energy Lett 2021;6:3864–72.
[50] Cho J, Mathew PS, DuBose JT, et al. Photoinduced halide segregation in Ruddlesden-Popper 2D mixed halide perovskite films. Adv Mater 2021;33:e2105585.
[51] Yan L, Ma J, Li P, et al. Charge-carrier transport in quasi-2D ruddlesden-popper perovskite solar cells. Adv Mater 2021;34:e2106822.
[52] Shi J, Gao Y, Gao X, et al. Fluorinated low-dimensional ruddlesden-popper perovskite solar cells with over 17% power conversion efficiency and improved stability. Adv Mater 2019;31:e1901673.
[53] Lin Z, Zhang Y, Gao M, et al. Kinetics of moisture-induced phase transformation in inorganic halide perovskite. Matter 2021;4:2392–402.
[54] Fan J, Ma Y, Zhang C, et al. Thermodynamically self-healing 1D–3D hybrid perovskite solar cells. Adv Energy Mater 2018;8:1703421.
[55] Duan H-S, Zhou H, Chen Q, et al. The identification and characterization of defect states in hybrid organic-inorganic perovskite photovoltaics. Phys Chem Chem Phys 2015;17:112–6.
[56] Gu X, Xiang W, Tian Q, et al. Rational surface-defect control via designed passivation for high-efficiency inorganic perovskite solar cells. Angew Chem Int Ed 2021;60:23164–70.
[57] Yang S, Chen S, Mosconi E, et al. Stabilizing halide perovskite surfaces for solar cell operation with wide-bandgap lead oxysalts. Science 2019;365:473–8.
[58] Xing J, Wang Q, Dong Q, et al. Ultrafast ion migration in hybrid perovskite polycrystalline thin films under light and suppression in single crystals. Phys Chem Chem Phys 2016;18:30484–90.
[59] Xi J, Spanopoulos I, Bang K, et al. Alternative organic spacers for more efficient perovskite solar cells containing ruddlesden-popper phases. J Am Chem Soc 2020;142:19705–14.
[60] Zhong Y, Liu G, Su Y, et al. Diammonium molecular configuration-induced regulation of crystal orientation and carrier dynamics for highly efficient and stable 2D/3D perovskite solar cells. Angew Chem Int Ed 2022;61:e202114588.

Yutian Lei is currently a M.S. student at Lanzhou University. His main research focuses on 2D optoelectronic materials and devices.

Zhenhua Li received his Ph.D. degree from Renmin University of China in 2014. He joined Lanzhou University in 2019. His research interest includes strongly correlated coupling systems and the simulation of the electronic structure of materials.

Zhiwen Jin received his Ph.D. degree from Institute of Chemistry, Chinese Academy of Sciences in 2016. He joined Lanzhou University in 2018. His research interest includes inorganic semiconductor materials, thin-film photoelectric devices and device physics.